Journal of Hazardous Materials 501 (2026) 140882

Contents lists available at ScienceDirect

Journal of Hazardous Materials

journal homepage: www.elsevier.com/locate/jhazmat

Cu(I)/Cu(II) dual-site mediated efficient synergistic catalysis of ozone and ethyl acetate

Xinge Li [a,b], Guanqing Song [a,b], Xiao Wang [a], Kaihuang Zhu [a], Shijie Yang [a,b], Guanhong Lu [a], Gansheng Shi [a], Xiaomeng Ren [c,*], Xinhong Xu [c], Jing Sun [a], Yan Wang [a,*]

[a] State Key Laboratory of High Performance Ceramics, Shanghai Institute of Ceramics, Chinese Academy of Sciences, 585 Heshuo Road, Shanghai 201899, China
[b] University of Chinese Academy of Sciences, 19 (A) Yuquan Road, Beijing 100049, China
[c] Navy Medical Centre, 880 Xiangyin Road, Shanghai 200433, China

HIGHLIGHTS

- CB-50 achieves 80 % EA and 77 % O_3 removal efficiency at room temperature , simultaneously.
- Acetic acid modulation introduces structural defects in Cu-BTC.
- Dual-site mechanism: Cu(I) activates O_3 and Cu(II)-OH adsorbs EA.

GRAPHICAL ABSTRACT

The dual-site synergistic mechanism of O_3 on Cu(I) sites and EA on Cu(II) sites have been elucidated. The low-valent metal sites of MOFs is the key point for O_3 activation.

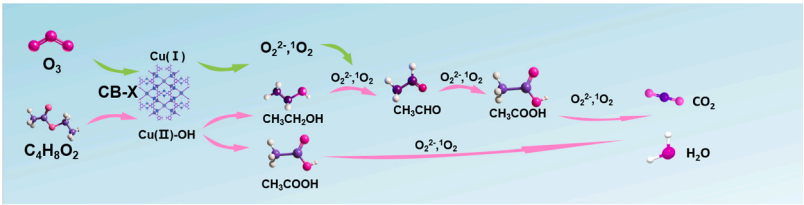

ARTICLE INFO

Keywords:
Synergistic catalysis
Cu-BTC
Defect engineering
Ethyl acetate
Ozone

ABSTRACT

In chip manufacturing facilities, high concentrations of ethyl acetate (EA) coexist with low concentrations of ozone (O_3), and achieving their simultaneous removal remains challenging. In this study, defect-engineered Cu-BTC MOF was employed for the room-temperature removal of EA and O_3 via synergistic catalysis. The CB-50 sample, synthesized with 50 μL acetic acid, achieved 80 % EA removal efficiency and 77 % O_3 removal efficiency, markedly higher than pristine Cu-BTC (60 % and 72 %). Meanwhile, EA mineralization reached 90.3 %, which is 1.3 times that of pristine Cu-BTC (69.6 %). XPS and *in-situ* DRIFTS analyses revealed that Cu(I) sites served as active sites for O_3 activation to yield •OH and O_2^{2-} species, whereas Cu(II)-OH groups acted as the adsorption sites for EA, facilitating its transformation into carboxylic intermediates. Using the same approach, defects were introduced into a series of representative MOFs, confirming the feasibility of regulating the content of low-valent metal sites via defect engineering. This dual-site mechanism facilitates the synergistic catalysis of EA and O_3. It demonstrates a promising strategy with potential for application of MOFs materials in room-temperature catalytic treatment of mixed gaseous pollutants.

1. Introduction

EA is extensively employed in electronics and chip manufacturing as a photoresist solvent and cleaning agent. Meanwhile, processes such as UV lithography [1,2], plasma treatment [3,4], and corona discharge [5,6] frequently release O_3. Consequently, the coexistence of EA and O_3 is

* Corresponding authors.
E-mail addresses: 173464411@qq.com (X. Ren), wangyan@mail.sic.ac.cn (Y. Wang).

https://doi.org/10.1016/j.jhazmat.2025.140882
Received 30 September 2025; Received in revised form 6 December 2025; Accepted 18 December 2025
Available online 18 December 2025

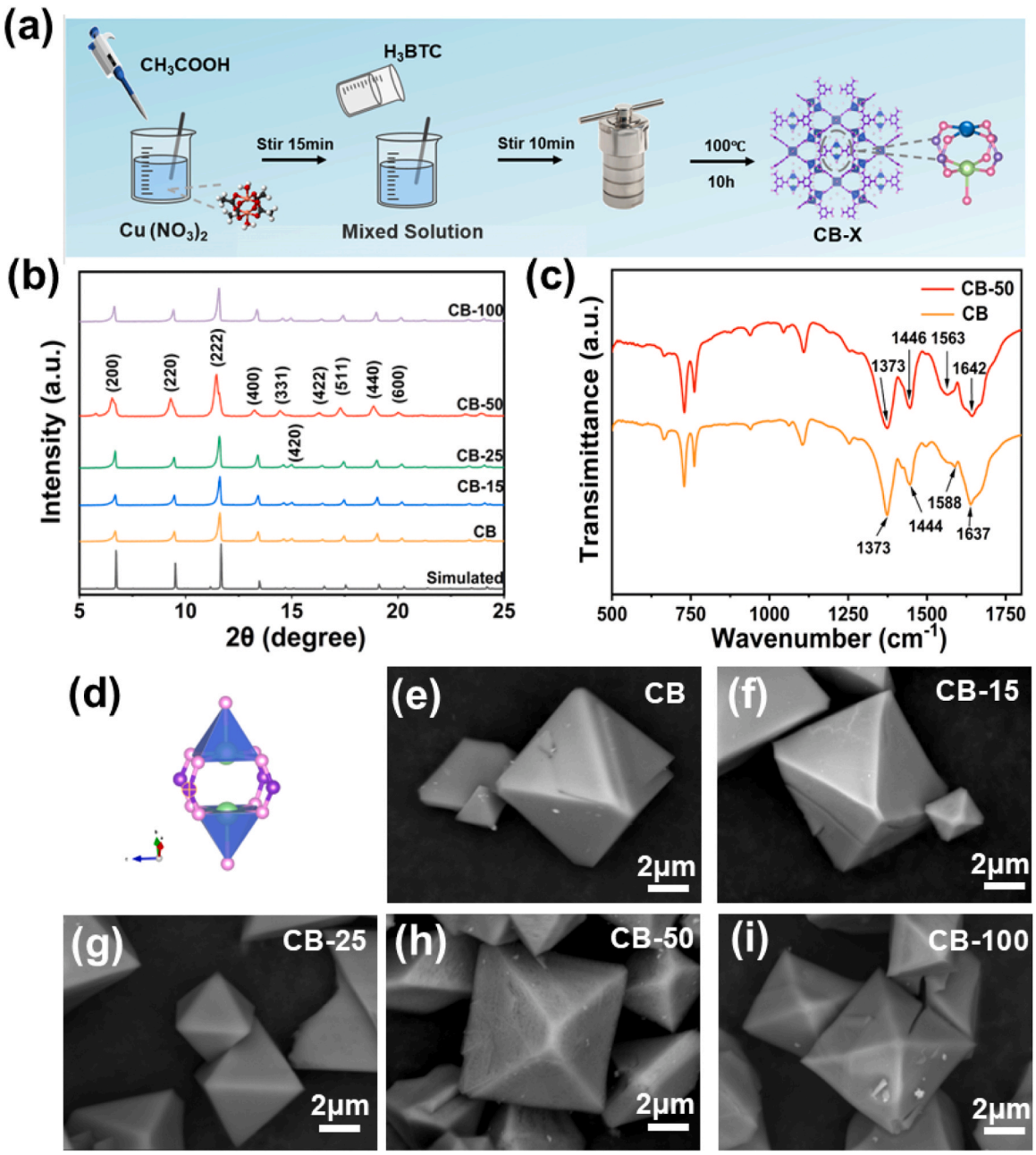

Fig. 1. (a) Synthesis process of CB-X (b) XRD patterns of CB-X. (c) FT-IR spectrum of CB-50 and CB; (d) Paddlewheel structure of Cu-BTC, SEM images of (e) CB, (f) CB-15, (g) CB-25, (h) CB-50 and (i) CB-100.

common, and the activation of O_3 into reactive oxygen species (ROS) has been established as an effective route for the abatement of oxygenated volatile organic compounds (OVOCs). [7–10] Higher O_3 concentrations facilitate the generation of ROS, leading to enhanced OVOC degradation efficiencies, particularly when the O_3-to-VOCs ratio exceeds unity. However, the O_3-to-VOCs ratio is generally less than unity under practical operating conditions. [11–13] Therefore, achieving the removal of high-concentration EA in the presence of low concentrations of O_3 is particularly difficult. In this process, efficient O_3 activation and utilization are essential to maximize ROS formation and achieve effective synergistic catalysis. [17]

The identification of active sites for O_3 activation is still contentious, with previous studies suggesting either oxygen vacancies (V_o) [14] or low-valent metal centers such as Cu^+ as the dominant contributors. [15, 16] Such uncertainty obscures mechanistic understanding and limits the rational design of catalysts. To date, most related studies have relied on metal oxides as catalysts. However, their limited ability to activate and utilize O_3 required a high O_3-to-pollutant ratio to achieve satisfactory performance. [16,17] Therefore, clarifying the active sites of O_3 activation and advancing catalyst design beyond conventional metal oxides are crucial for achieving efficient OVOCs removal at low O_3 concentrations.

Metal–organic frameworks (MOFs), owing to their large surface areas, well-defined porosity, and structural tunability, have emerged as highly promising catalytic materials. In addition, Cu(I) sites can efficiently activate O_3, while Cu(II) sites adsorb EA through coordination with its C═O groups. [18–20] Consequently, Cu-BTC, a representative Cu-based MOF, can be engineered with defects through chemical modulation [21] or thermal treatment [22]. This allows regulation of the Cu (I)/Cu(II) ratio and makes it a promising candidate for the synergistic catalysis of EA and O_3.

Inspired by the above ideas, for the first time, we employed defect-

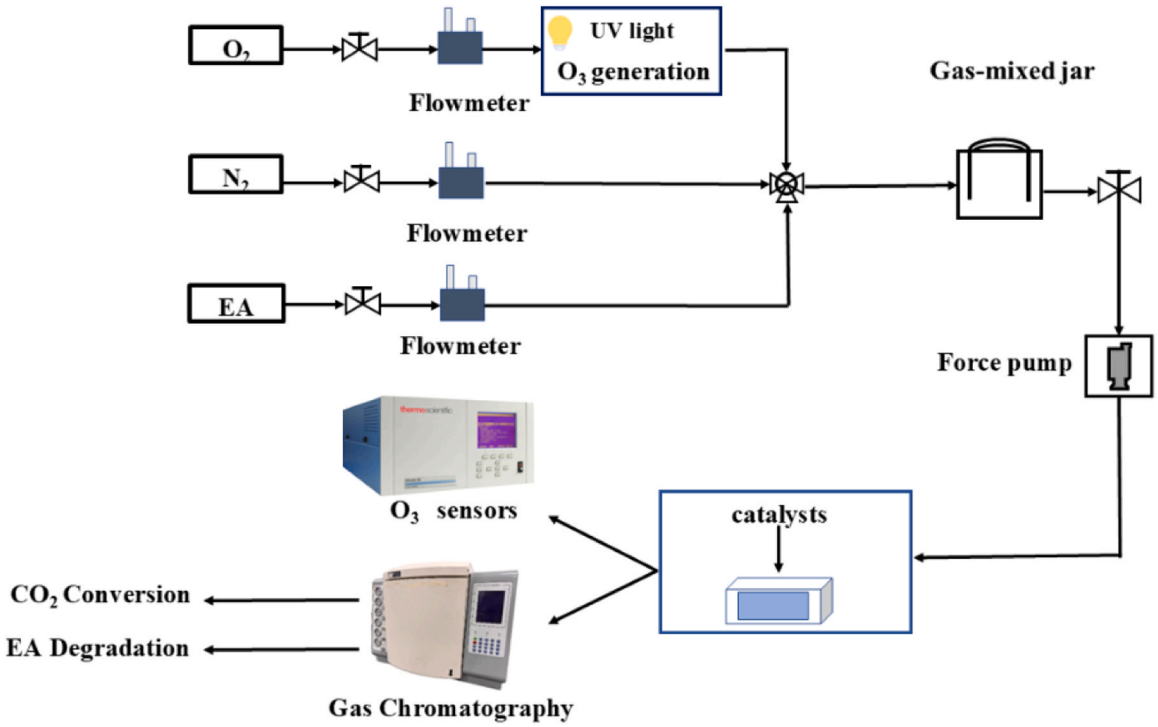

Scheme 1. Schematic diagram of mobile phase ozone degradation test system.

engineered Cu-BTC for the synergistic catalysis of EA and O_3. The defect amount was tuned by introducing different volumes of acetic acid (15 μL, 25 μL, 50 μL and 100 μL) to adjust the ratio of the Cu(I)/Cu(II). The relative contents of Cu(I) and Cu(II) were determined through peak deconvolution of XPS spectra. The experimental results revealed that an increase in Cu(I) content improved both O_3 and EA removal efficiencies. The dual-site roles of Cu(I) and Cu(II) were confirmed by XPS analysis, while the interactions between O_3/Cu(I) sites and EA/Cu(II) sites during the catalytic process were elucidated by *in-situ* DRIFTS. When the Cu(I)/Cu(II) ratio reached 1.88, the catalyst exhibited the highest EA removal efficiency within 60 min, reaching 80 %. At the same time, the efficiency of O_3 activation to ROS was maximized at 77 %. Finally, PTR-TOF-MS was employed to elucidate potential synergistic catalytic pathways in the EA/O_3 system by tracking real-time volatile intermediates and products.

2. Experiment

2.1. Catalyst Preparation

2.1.1. Materials

Copper (II) nitrate trihydrate, trimesic acid (H_3BTC), N, N-dimethylformamide (DMF) and ethanol were obtained from Shanghai Adamas Reagent Co., Ltd. Acetic acid was purchased from Sinopharm Chemical Reagent Co., Ltd. Deionized water was prepared using an ultrapure water system (Shanghai, Tondino Scientific Co., Ltd). All reagents were used without further purification.

2.1.2. Synthesis of Cu-BTC

Cu-BTC was prepared via a solvothermal method. First, 1.0 g (4.8 mmol) of H_3BTC was dissolved in a mixed solution of 15 mL DMF and 15 mL ethanol. 2.07 g (8.6 mmol) of Cu $(NO_3)_2{\cdot}3\ H_2O$ was dissolved in 15 mL deionized water separately. The two solutions were mixed, stirred and transferred to a 100 mL Teflon-lined stainless-steel autoclave. It was heated at 100 °C for 10 h. The resulted blue precipitate was collected by centrifugation, washed three times with DMF and ethanol, and dried under vacuum at 80 °C for 6 h to get Cu-BTC (denoted as CB).

2.1.3. Synthesis of CB-X

To introduce structural defects, varying volumes of acetic acid (15, 25, 50 and 100 μL) were added to the metal precursor solution while maintaining all other synthesis parameters identical to those of Cu-BTC. The resulting samples were denoted as CB-X, where X corresponds to the volume of acetic acid added. All CB-X samples were vacuum dried at 120 °C for 12 h to remove residual solvent molecules from the pores. (Fig. 1a)

2.2. Characterization

XRD profiles were carried out on the D8 ADVANCE (Germany Bruker Corporation) with a Cu anode at 40 kV, 20 mA. The Cu Kα (λ=1.5418 Å) was selected as the source of diffraction. The scanning range was 5–50°, and scanning rate was 2° /min. XPS spectra studies were conducted on Thermo Scientific K-Alpha. The Al Kα was selected as the incident source, the energy step size was 1 eV and the scanning range was 0–1200 eV. All of XPS peaks were referenced to the C 1 s signal at 284.8 eV. Nitrogen adsorption-desorption test was carried out by JW-BK200 at 77 K (JWGB Sci & Tech Ltd). The samples were heat treat at 120 ℃ under vacuum to eradicate the residual gases before test. Fourier Transform Infrared (FT-IR) spectra were measured on a Nicolet iS50 spectrometer with a 4000–400 cm^{-1} resolution of 4 cm^{-1}. The test conditions were same as the corresponding target gases degradation. The PTR-TOF-MS was conducted on Ionicon PTR-TOF 6000 × 2. After degradation for one hours, the reaction gas was collected, diluted 1000-fold with N_2 and flowed into the PTR-TOF- MS to detect the degradation products. The ESR was measured by Bruker EMXNANO (Germany). The powder samples were transferred into fine quartz tubes and subsequently placed in an electron paramagnetic resonance spectroscopy spectrometer to test for oxygen vacancies in the materials. In-situ Transform spectroscopy (in-situ DRIFTS) data were measured with an IR Tracer-100 (Shimadzu, Japan). The dome of the reaction cell was equipped with 2 KBr windows designed for IR transmission and a quartz window for extra light illumination. The spectra were displayed in the transmission mode and obtained with a resolution of 8 cm^{-1} through 45 scans. The specific test steps of the in-situ DRIFTS measurement were as

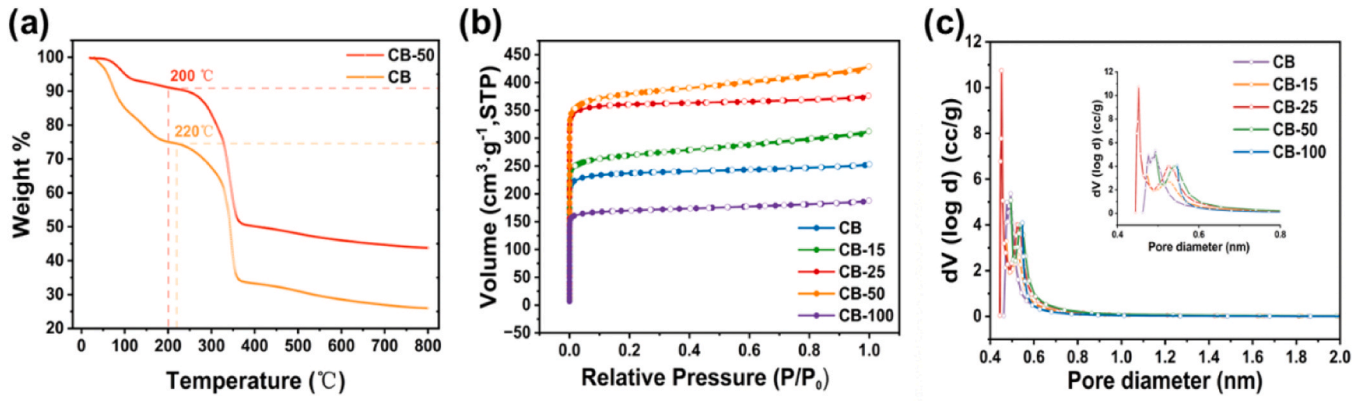

Fig. 2. (a) TG curves of CB and CB-50 under N_2 atmosphere. (b) N_2 adsorption-desorption isotherms at 77 K and (c) corresponding pore distribution curves of CB, CB-15, CB-25, CB-50, CB-100.

follows: Firstly, the sample was placed in an in-situ reaction cell with a quartz window, and the reaction cell was sealed. Then, the sample was subjected to desorption under a N_2 atmosphere at room temperature for 30 min. Thereafter, EA and O_3 were simultaneously introduced into the reaction cell. The DRIFTS spectra were recorded every 3 min to investigate the synergistic catalytic reaction. The inlet O_3 concentration was set at 10 ppm with a flow rate of 13 sccm. EA was introduced at 100 ppm with a flow rate of 7 sccm.

2.3. Adsorption and catalytic ozonation performance

Adsorption and synergistic catalysis tests for ethyl acetate and ozone were conducted in a gas-solid phase catalytic system (Scheme 1) [23]. A suspension was prepared by dispersing 50 mg of catalyst in 3 mL ethanol and sonicating for 5 min. The resulting mixture was uniformly coated onto a glass pane (15 cm × 7 cm) and heated at 80 °C for 20 min to completely evaporate the solvent. The coated substrate was then placed in the reaction chamber. Ozone flow was precisely controlled by adjusting the oxygen intake and the ozone generator, with concentrations monitored by an ozone analyzer and four flowmeters. In this study, the inlet ozone concentration was set at 10 ppm. Ethyl acetate was introduced at 100 ppm with a flow rate of 140 sccm for both adsorption and catalytic experiments. Total gas flow rate was 1.4 L/min. The cyclic experiments were carried out under the same procedure.

The concentration of CO_2 produced by VOCs during ozonation degradation was detected by GC-FID (GC-7920, Beijing China Education Au-light Co., Ltd), equipped with nickel-based catalyst to convert low concentration CO_2 to methane. The specific test method was as follows. The gas of N_2:O_2 = 4:1 was applied to replace air to eliminate the influence of CO_2 in the air on the test results. The whole gas path and the reaction chamber were purged with N_2 until no CO_2 peak was detected. CO_2 (200 ppm) gas was used as the standard gas to calibrate the peak area of CO_2. At the beginning, the catalyst was placed in the reaction chamber and purged the reaction chamber with N_2 until no CO_2 peak was detected in the whole gas path.

The mineralization rate was calculated by the formula added in the revised supporting information as follow. [24]

$$\eta_{CO_2} = \frac{C_{CO_2}}{C_{VOCs} \times \eta \times n} \times 100\% \quad (1)$$

Where C_{CO_2}(ppm) represents the amount of CO_2 generated in the photocatalytic process, and C_{VOCs} (ppm) stands for the amount of EA total inflow. η is the synergistic catalysis removal efficiency, and n represents the carbon number in EA.

Table 1
The physical structural properties of CB-X.

Samples	S_{BET}[a](m^2/g)	V_{total}[b](cm^3/g)	V_{micro}[c](cm^3/g)	V_{meso}[d](cm^3/g)
CB	825.47	0.390	0.352	0.038
CB-15	937.59	0.481	0.372	0.109
CB-25	1255.74	0.580	0.546	0.034
CB-50	1321.86	0.661	0.539	0.122
CB-100	591.80	0.289	0.246	0.043

[a] BET specific surface
[b] Total pore volume measured at $P/P_0 = 0.99$
[c] Micropore volume calculated using the t-plot method
[d] Mesopore volume calculated using the t-plot method

3. Results and Discussion

3.1. Catalyst Characterization

Fig. 1a presented the synthesis process of the CB-X series catalysts. The result of XRD was shown in Fig. 1b. All of samples showed similar diffraction patterns, and conformed to simulated Cu-BTC diffraction patterns. In the spectrum of the CB sample (Fig. 1b), two minor peaks at 14.6° and 15.0° were ascribed to the (331) and (420) planes of CB, respectively. After the addition of 50 μL acetic acid, the CB-50 only exhibited a solitary minor peak near 14.4°. The disappearance of the peak signal at 15.0° implied that CB-50 only contained a negligible amount of absorbed water, while CB was found in a hydrated state. [25] The broader diffraction peaks observed in CB-50 indicated a decrease in crystallite size [26]. This was attributed to acetic acid disrupting the coordination of trimesic acid with Cu centers during synthesis, thus inhibiting further crystal growth. Fig. 1c presented the FT-IR spectrum of CB and CB-X catalysts, all of which were in agreement with literature reports for Cu-BTC. [27] The two bands in the 1370–1460 cm^{-1} region and the pair of absorptions between 1580 and 1650 cm^{-1} were assigned to the symmetric and asymmetric stretching modes of carboxylate groups [28], confirming the successful synthesis of Cu-BTC. SEM was utilized to explore the morphology of CB-X. As demonstrated in Fig. 1e-i, both CB-X exhibited octahedral morphologies. [29,30] These results demonstrated that the addition of a small amount of acetic acid did not alter the framework structure of Cu-BTC, with the morphology of the CB-X series catalysts well preserved.

The thermogravimetric analyses (TG) were used to investigate the thermal stability of CB and CB-50. As shown in Fig. 2a, the CB sample began to decompose at around 220 °C, whereas the CB-50 exhibited decomposition at 200 °C. This indicated that CB-50 possessed lower thermal stability. BET measurements were conducted to investigate the influence of acetic acid on physical structural properties. The N_2

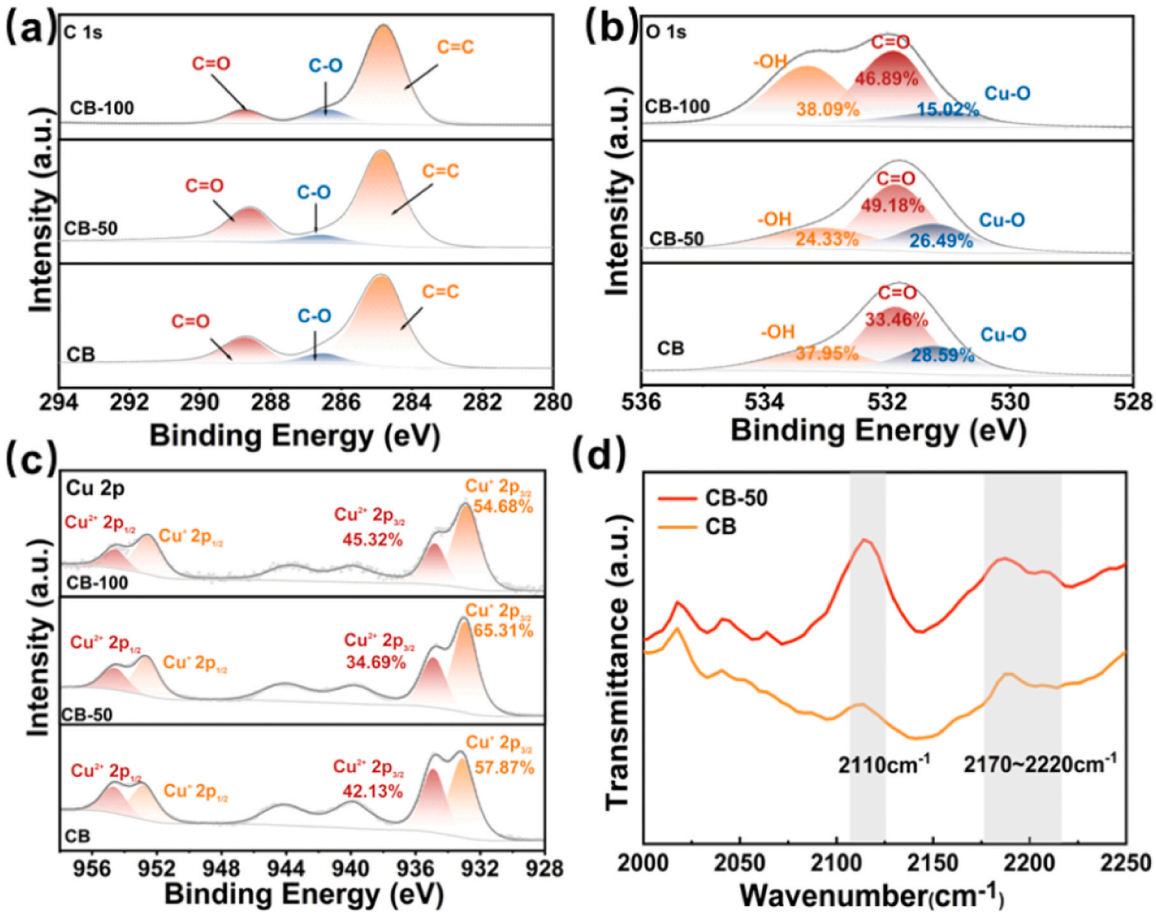

Fig. 3. X-ray photoelectron spectroscopy curves of (a) C, (b) O and (c) Cu elements of CB, CB-50 and CB-100; (d) CO *in-situ* DRIFTS of CB and CB-50.

adsorption isotherms of all samples displayed a type I with a rapid uptake at $P/P_0 < 0.1$ and no discernible hysteresis loop was observed (Fig. 2b). This indicated a predominance of micropores, with slight meso-/macropores structure [31]. Table 1 showed that increasing the amount of acetic acid led to higher specific surface area and pore volume, with CB-50 exhibiting the maximum surface area of 1321.86 m^2/g. Conversely, CB-100 demonstrated a minimal surface area of 591.80 m^2/g, which was probably attributable to structural collapse resulted from excessive acid. Consistent with this observation, the pore distribution curves (Fig. 2c) revealed that CB-50 exhibited the largest pore volume and average mesopore diameter due to the partial loss of organic ligands, confirming the effectiveness of the defect-engineering strategy. The introduction of defects lowered the coordination number of the metal clusters, which in turn induced the formation of Cu(I) species. This was further corroborated by XPS analysis of Cu(I) content (Fig. 3c). Among the CB-X catalysts, CB-50 contained the highest percentage of Cu(I) species at 65.31 %, while CB exhibited the lowest at 57.87 %. These results indicated that Cu(I) content was closely correlated with the structural properties, and its enhancement originated from defect generation.

XPS analyses provided further insight into the elemental states and compositional changes. The C 1 s spectra (Fig. 3a) displayed peaks at 284.8 eV, 286.48 eV, and 288.7 eV, corresponding to C-C, C-O, and C═O bonds, respectively. [32] The O 1 s spectrum of CB (Fig. 3b) revealed peaks at 531.34 eV, 531.93 eV, and 532.93 eV, which were attributed to Cu-O, C═O, and -OH bonds. [31] Notably, the relative content of the Cu-O bond in CB-50 decreased from 28.59 % to 26.49 %. This reduction arose from the introduction of acetic acid, which initially substituted for trimesic acid in coordination and was later removed at 100 °C, thereby creating coordination vacancies. This conclusion was further supported by the Cu 2p spectra (Fig. 3c). For the CB catalyst, the peaks at 933.10 eV and 934.89 eV were assigned to Cu^+ and Cu^{2+} with relative abundances of 57.87 % and 42.13 %. In CB-50, the Cu^+ peak shifted to 932.88 eV, indicating ligand deficiency and alteration in the copper coordination environment. [33] Moreover, as the amount of acetic acid increased, the Cu^+/Cu^{2+} ratio rose from 1.37 to 1.88. This trend highlighted that defect formation increased the proportion of Cu^+ species, evidencing the abundance of defect sites in CB-X (Figure S3). The increase in Cu^+ was accompanied by a decrease in -OH content, as observed in the O 1 s spectra. [34] For Cu(II), the coordination mode was $Cu(II)_2(RCOO)_4$, with four carboxylic acid linkers coordinated to the dinuclear cation cluster and a -OH hydroxyl group coordinated in the axial position. The transition from Cu(II) to Cu(I) led to an increase in local electron density at Cu(I) sites [35], weakening their coordination ability. This change in coordination mode led to the formation of $Cu(I)_2(RCOO)_2$, which was unable to coordinate with the hydroxyl group. Consequently, the content of -OH bonds in CB-50 was reduced by 13.62 % compared to the CB sample (Table 1), while CB-100 exhibited the highest -OH content and the lowest Cu^+ content. To gain further insight into the abundance of Cu^+ sites, *in-situ* DRIFTS with CO as a probe was conducted on both CB and CB-50. As illustrated in Fig. 3d, both samples manifested prominent CO adsorption peaks at 2110 cm^{-1} and within the 2170–2220 cm^{-1} range, which can be attributed to Cu^+-CO and Cu^{2+}-CO interactions, respectively. The CB-50 sample displayed a more evident peak at 2110 cm^{-1}, indicating a higher concentration of defective Cu^+ sites. [36]

3.2. Catalytic Ozonation Performance

Synergistic catalysis experiments were carried out at room

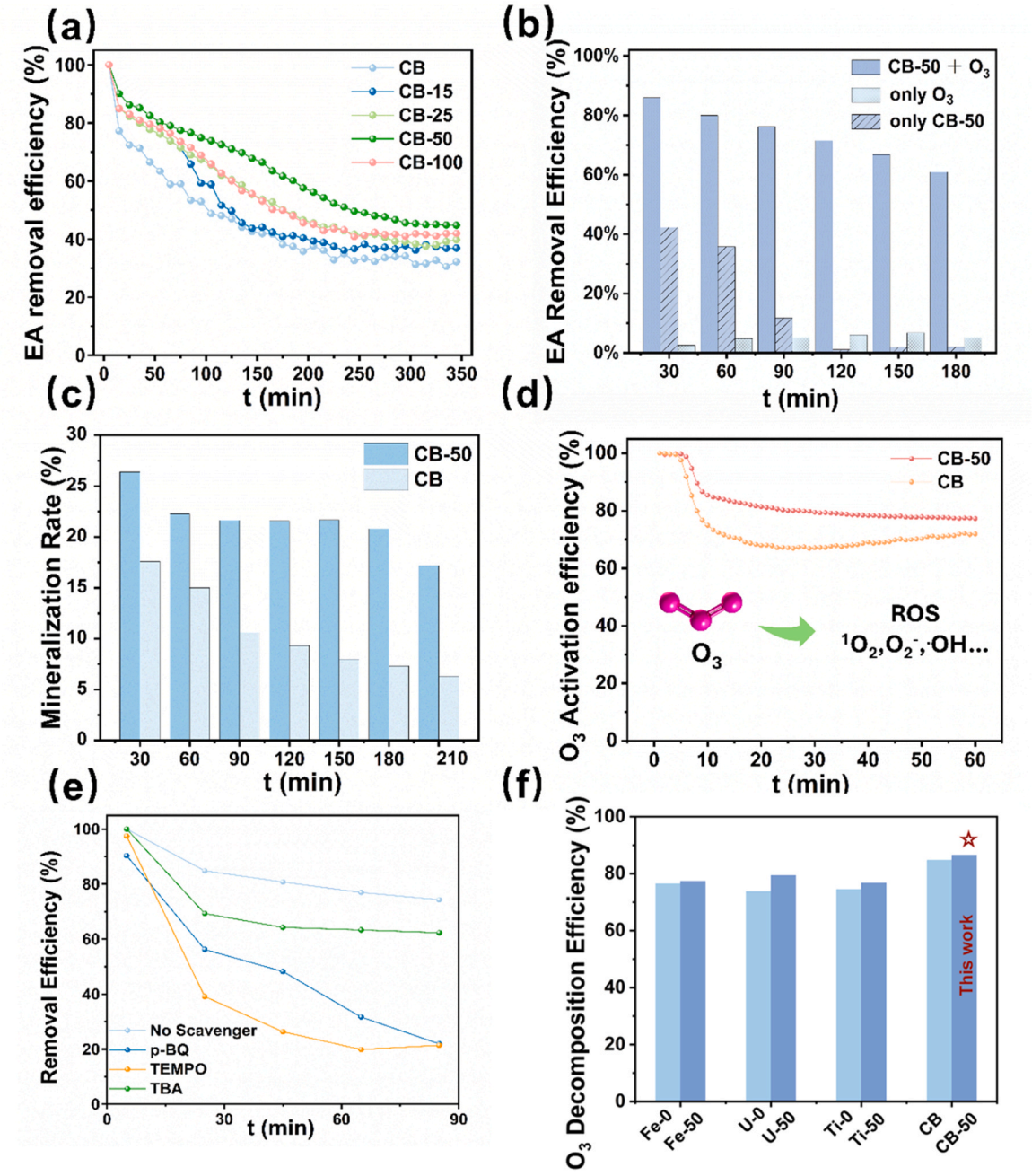

Fig. 4. (a) Synergistic catalytic performance of CB-X catalysts. (b) Control experiment of CB-50. (c) EA mineralization rate of CB and CB-50. (d) Simultaneous monitoring of EA removal efficiency and O_3 concentration in the tail gas of CB-50 and CB. (e) The trapping experiment over CB-50 during synergistic catalysis of EA. (f) General applicability of low-valent metal sites in MOFs for O_3 decomposition within 90 min.

Table 2
The XPS analysis of CB-X.

Samples	Cu(I)	Cu(II)	Cu(I)/Cu(II)	-OH
CB	57.87 %	42.13 %	1.37	37.95 %
CB-15	59.74 %	38.63 %	1.59	26.67 %
CB-25	61.06 %	34.79 %	1.87	33.16 %
CB-50	65.31 %	34.69 %	1.88	24.33 %
CB-100	59.60 %	45.32 %	1.21	46.03 %

temperature in a gas-solid flow reactor with inlet concentrations of 100 ppm EA and 10 O_3 (EA: O_3 = 10:1). As shown in Fig. 4a, among all samples, CB-50 showed the best performance, with an EA removal efficiency of 86.0 % at 30 min and 45.1 % at 350 min. In contrast, CB-15, CB-25, and CB-100 reached 81.4 %, 81.5 %, and 82.1 % at 30 min, stabilizing at 37.1 %, 38.7 %, and 40.8 % at 350 min. The pristine CB exhibited the lowest efficiency, decreasing from 71.7 % at 30 min to 32.2 % at 350 min. Such inferior performance was mainly ascribed to the minimal specific surface area and the relatively low Cu(I) content (Table 2). The continuous decline in removal efficiency was attributed to the gradual oxidation of active Cu(I) sites in CB-X to Cu(II) during the reaction. Compared with previous studies that focused on thermal catalysis for EA abatement, this work achieved efficient EA removal under ambient conditions. Meanwhile, the EA-to-O_3 concentration ratio was maintained below unity, demonstrating that effective EA oxidation can be achieved with minimal O_3 consumption in the catalytic system. Fig. 4b compared the EA removal efficiencies over 180 min under different conditions, CB-50 + O_3, O_3 (oxidation) or CB-50 (physical

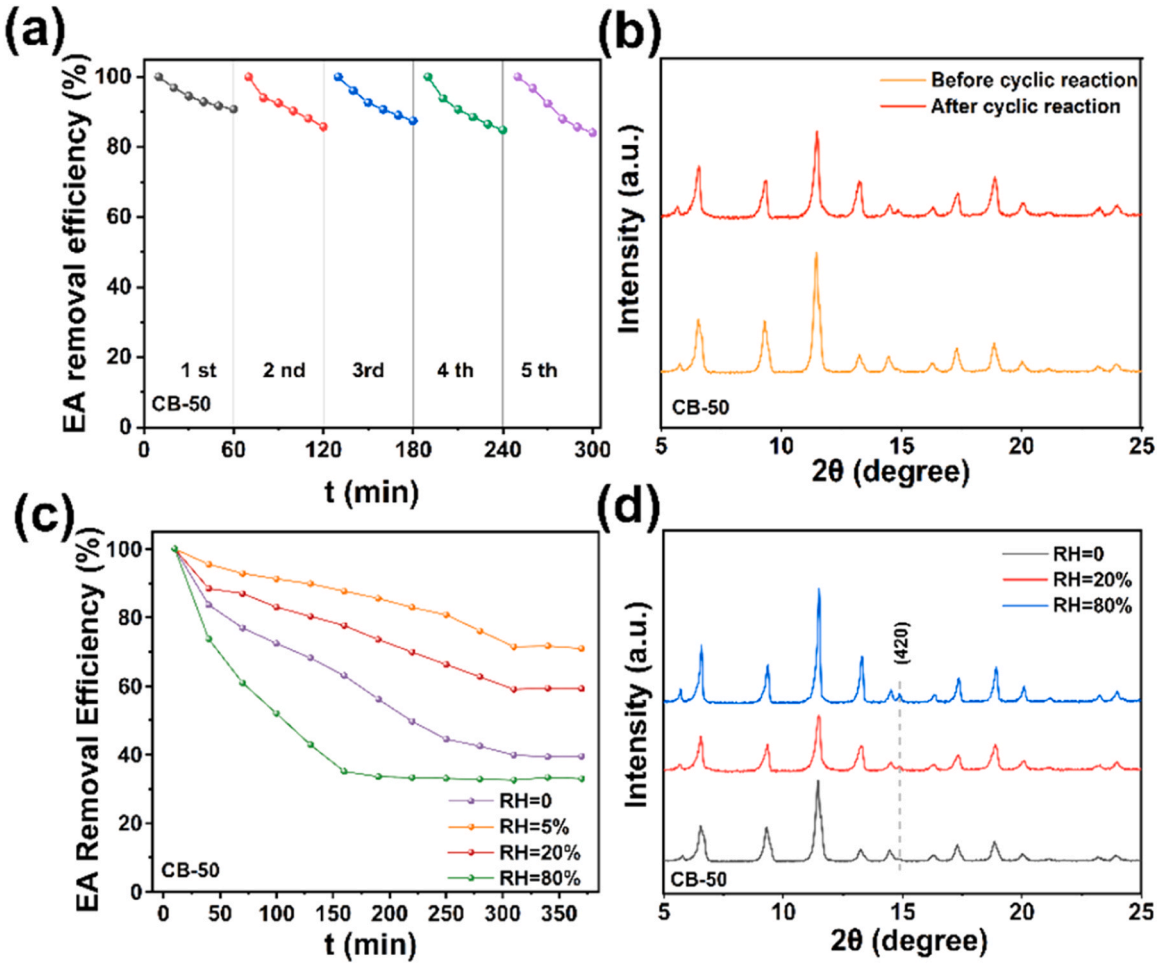

Fig. 5. (a) The cyclic experiment of CB-50. (b) XRD patterns of CB-50 before and after cyclic experiments. (c) The EA removal efficiency of CB-50 at different humidity. (d) The XRD patterns of CB-50 after synergistic catalytic reaction under different relative humidity.

adsorption). Control experiments indicated that both oxidation and physical adsorption exerted negligible effects on EA removal due to the efficiencies of 1.1 % and 6.1 % respectively. These results demonstrated the necessity of the synergistic interaction between the catalyst and O_3 for effective abatement. To exclude the influence of surface area on the catalytic performance, the normalized initial reaction rates of CB-X (Table S1) have been calculated. [37] The normalized rate of CB-50 was $r = 2.32 \times 10^{-3}$mol·m^{-2}·s^{-1}, which is higher than that of CB ($r = 2.15 \times 10^{-3}$mol·m^{-2}·s^{-1}). This indicates that the superior synergistic catalytic performance of CB-50 may result from the combined effects of its larger surface area and the presence of dual active sites.

The mineralization of EA was determined by monitoring the CO_2 concentration produced during the *in-situ* synergistic catalytic rection at room temperature (Fig. 4c). EA mineralization was significantly enhanced by CB-50, reaching 26.4 % within 30 min, compared to 17.6 % over CB. Due to Cu-BTC possessed a large surface area and high porosity, they easily adsorbed CO_2 generated during EA mineralization. CO_2-TPD of CB-50 also proved CO_2 desorption occurred at 107 °C and 172 °C (Figure S1). Thus, CB and CB-50 after reaction was heated at 100 °C overnight in sealed chamber to release absorbed CO_2 (Figure S2). According to the Eq. 1, the EA mineralization rate of CB-50 is 90.3 % higher than that of CB (69.6 %). In addition, the O_3 concentrations in the effluent gases of CB and CB-50 were monitored to evaluate the O_3 removal efficiency (Fig. 4d). Within 60 min, the O_3 removal efficiency of CB was only 72.0 %, whereas that of CB-50 reached 77.3 %. These results demonstrated that CB-50 possessed stronger oxidation capability and superior synergistic catalytic performance compared with CB.

During the synergistic catalysis of EA and O_3, the generation of ROS was an important intermediate process. To explore the effect of various ROS on the catalytic process, the trapping experiment were carried out. P-benzoquinone (p-BQ) was used to trap •O_2^-, TEMPO was used to trap $^1O_2$ and tert-butanol (TBA) was used to trap·•OH radicals. As shown in Fig. 4e, the addition of TBA decreased EA removal efficiency from 74.3 % to 62.3 % over 85 min, indicating that •OH radicals have a minor role in the process. Under identical conditions, the addition of TEMPO and p-BQ resulted in a significant decrease in EA removal efficiency. Specifically, TEMPO reduced the efficiency from 74.3 % to 21.4 %, while p-BQ caused a decline from 74.3 % to 22.0 %. These findings indicate that $^1O_2$ and •O_2^- were the predominant reactive oxygen species in the catalytic process.

To verify the broader applicability of the defect-engineering strategy developed in this study, 50 μL of acetic acid was introduced during the synthesis of several representative MOFs, including Fe-BTC, UiO-66 and MIL-125(Ti). The pristine MOF samples without acetic acid were denoted as Fe-0, U-0 and Ti-0, whereas those synthesized with acetic acid were designated as Fe-50, U-50 and Ti-50 for distinction (SI 1 Experimental details). XPS analysis revealed that Fe-50 and Ti-50 exhibited an increased proportion of low-valent metal species compared with Fe-0 and Ti-0 (Figure S4). In the U-50 sample, the binding energy of the Zr $3d_{5/2}$ orbital showed a blue shift of 0.32 eV relative to U-0, indicating that the introduction of acetic acid induced electron withdrawal from Zr sites, thereby confirming the presence of defects in U-50. [33] As shown in Fig. 4f, all modified catalysts exhibited enhanced O_3 removal efficiency within 90 min, highlighting the

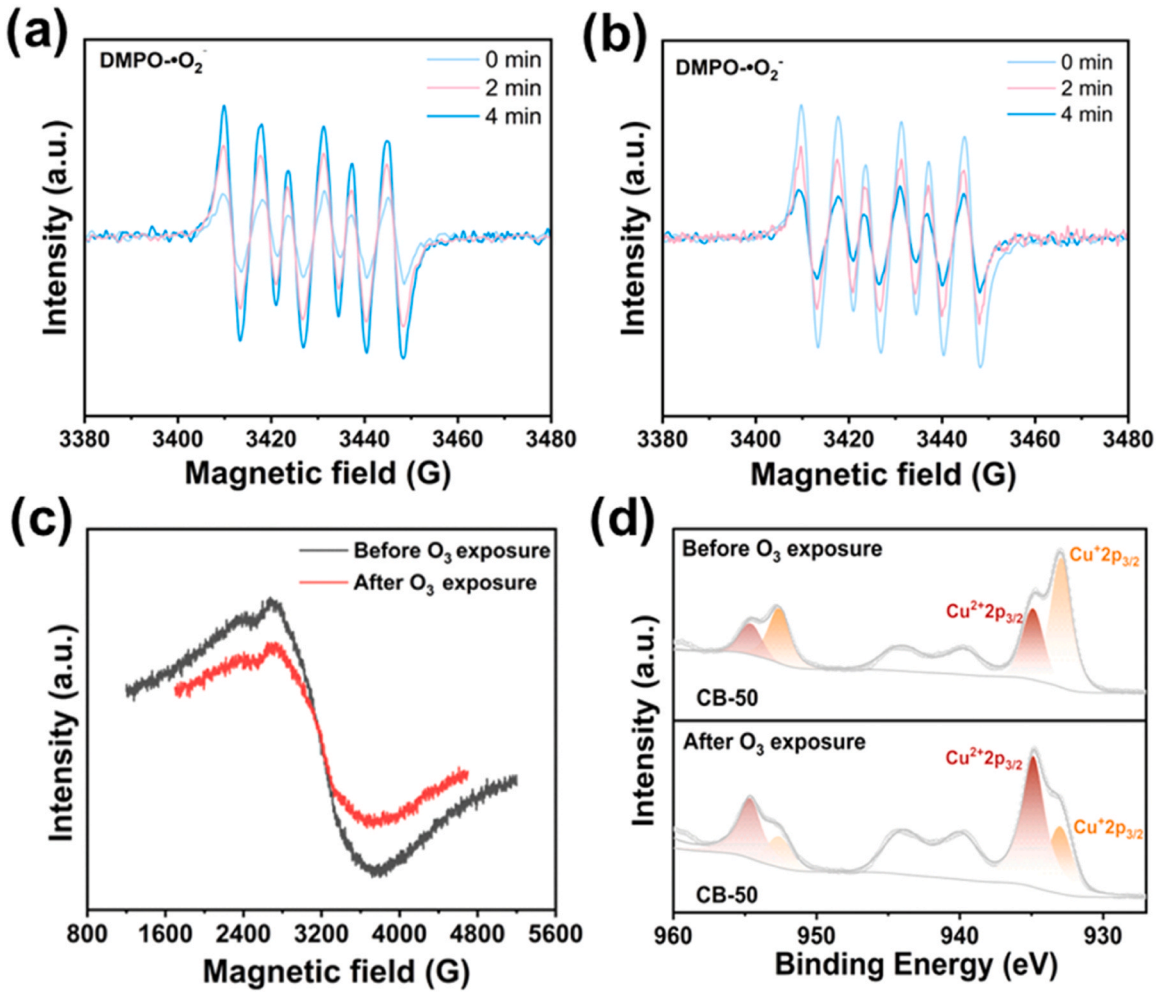

Fig. 6. (a) *in-situ* EPR spectra of DMPO-•O_2^- in the CB-50/O_3 system. (b) *in-situ* EPR spectra of DMPO-•O_2^- in the CB-50/O_3 + EA system (c) EPR spectra of Cu species in the CB-50/O_3 system (d) Cu 2p XPS spectra of CB-50 before and after exposure to O_3 within 60 min.

generality and significance of constructing low-valent metal centers via defect engineering in MOFs for synergistic catalysis of OVOCs and O_3. In addition, we also evaluated the synergistic catalytic performance toward EA of series MOF materials (Table S2). The results revealed that defect-engineered MOFs exhibited superior performance compared to pristine MOFs (Figure S5). This enhancement was attributed to the higher efficiency of O_3 decomposition and activation in the defect-rich structures, which strengthened the overall redox capability of the catalytic system. Among the series of MOF materials, the CB and CB-50 samples showed the highest catalytic activity.

The cyclic experiments were performed to evaluate the catalytic stability of CB-50 (Fig. 5a). The decrease in catalytic performance of CB-50 over 350 min can be ascribed to the oxidation of Cu(I) sites to Cu(II) during the reaction. To regenerate the Cu(I) species, the CB-50 after cyclic experiment was subjected to UV irradiation for 1 h. After the light-induced regeneration, the catalyst exhibited excellent stability over five consecutive cycles, maintaining an EA removal efficiency of 85 %. The XRD patterns revealed that the diffraction peaks of CB-50 remained same after cyclic experiments, indicating that the crystalline structure was well preserved (Fig. 5b).

Since water vapor is ubiquitous in industrial waste streams, it is essential to evaluate the stability of the catalyst under humid conditions. We conducted tests under different relative humidity levels (RH= 0, 5 %, 20 %, 80 %). As shown in Fig. 5c, the EA removal efficiency of CB-50 within 100 min increased from 72.4 % to 91.2 % and 83.0 % under low RH conditions (5 % and 20 %). This improvement may be attributed to the introduction of a small amount of water vapor, which can generate surface -OH groups and thereby strengthen EA adsorption. In addition, limited humidity can facilitate O_3 decomposition and promote the formation of ROS. [19,38,39] At 80 % RH, the EA removal efficiency of CB-50 decreased to 52.0 %, which may be resulted from the competitive adsorption of excessive water vapor that occupied the active sites of the catalyst.

To assess humidity stability, XRD patterns before and after the reaction were compared (Fig. 5d). The diffraction peak positions and intensities of all samples remained similar, indicating its good structural stability under humid conditions. Notably, as the humidity increased to 80 %, there are a new distinct hydration peak at 14.0°, which was water molecules occupied the active sites on the catalyst surface.

3.3. Mechanistic Insights

The *in-situ* EPR experiments have been conducted to validate the formation and evolution of ROS during the synergistic catalytic reaction (Fig. 6a-b). The results exhibited that the concentration of superoxide radicals (•O_2^-) gradually increased as the reaction time between CB-50 and O_3 increases from 0 min to 2 and 4 min (Fig. 6a). After EA was introduced into the reaction system, the •O_2^- reacted with EA, resulting in a decrease in the •O_2^- peak intensity (Fig. 6b). Furthermore, Cu valence evolution in CB-50 was monitored to characterize Cu(I) acted as the active site for O_3 (Fig. 6c). It showed that the characteristic Cu(II) signals became more pronounced in the EPR spectra, indicating that Cu

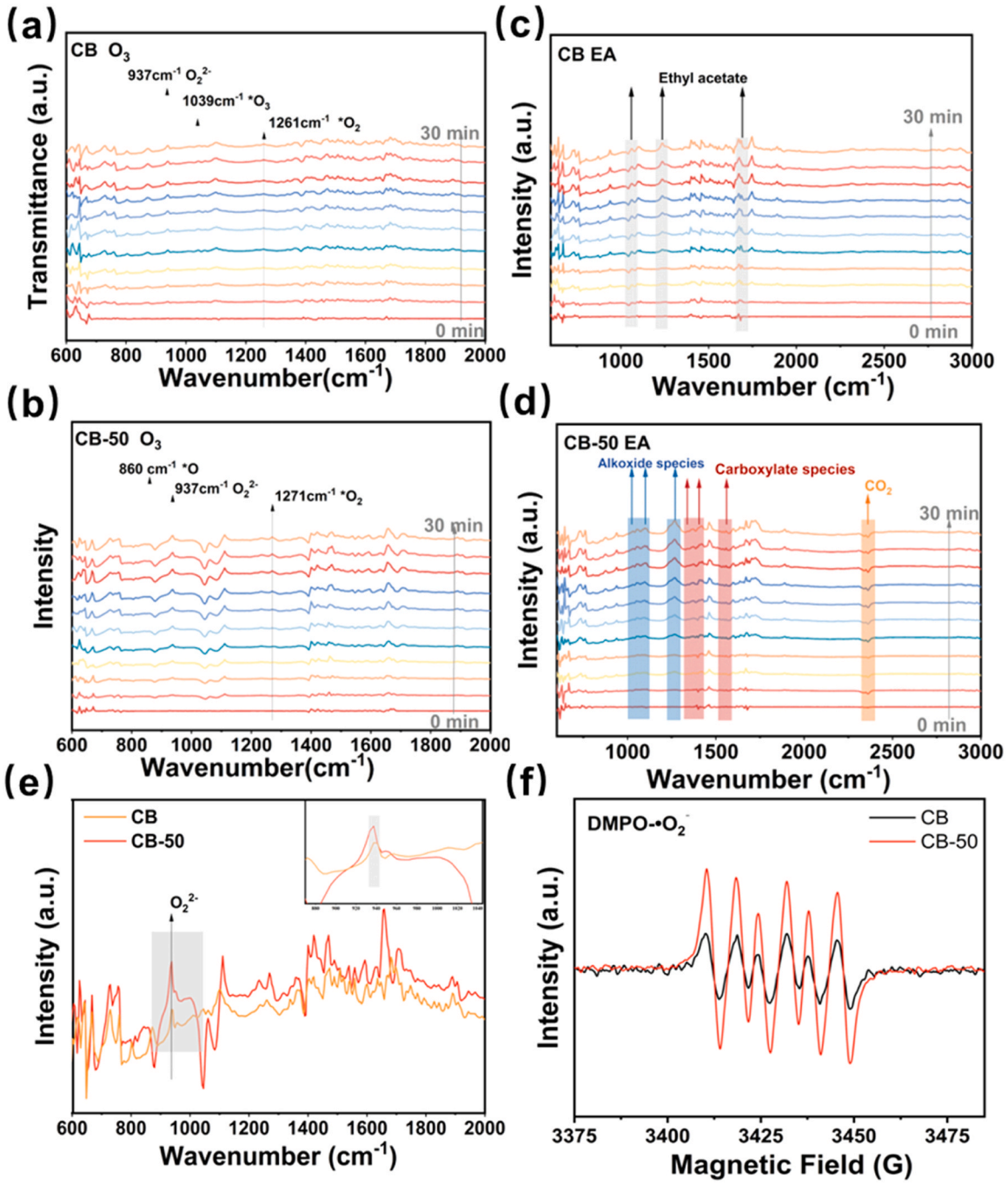

Fig. 7. *in-situ* DRIFTS of (a) CB (b) CB-50 under O_3/Air atmosphere and (c) CB (d) CB-50 under EA/Air atmosphere. (e) *in-situ* DRIFTS of CB and CB-50 under O_3/Air atmosphere for 30 min. (f) EPR spectrum of DMPO-•O^{2-}- over CB and CB-50 under O_3 atmosphere.

(I) was oxidized to Cu(II). [40] To further confirm this, XPS analysis was performed to investigate the changes in the oxidation states of Cu in CB-50 before and after exposure to O_3. As shown in Fig. 6d, the Cu(I) content decreased markedly from 65.31 % to 28.85 %, while the Cu(II) content increased from 42.13 % to 71.15 % after the reaction. This significant shift in copper oxidation states indicated that Cu(I), serving as the primary active site, facilitated the activation of O_3 into various reactive oxygen species via a Cu(I) → Cu(II) redox process. [15] Meanwhile, the variation in -OH groups of CB-50 before and after EA adsorption was monitored (Figure S6). The relative content of -OH decreased upon exposure to EA, which demonstrated that Cu(II)-OH groups served as the adsorption sites for EA. Since oxygen vacancies in the material were considered potential active sites for O_3 activation [14,16,41], EPR analysis was conducted to examine the changes in their concentration. As shown in Figure S7, no detectable EPR signals corresponding to oxygen vacancies were observed in either CB or CB-50, confirming their absence in the catalyst structure. Therefore, it can be concluded that the synergistic catalytic activity of CB-50 originated mainly from Cu(I) sites, rather than from oxygen vacancies.

In-situ DRIFTS measurements were carried out under O_3/air and EA/air atmospheres to investigate the adsorption of EA and O_3 on the CB and CB-50, aiming to elucidate the pathways of ROS generation and EA transformation. The adsorption behavior for O_3 exhibited significant disparities between CB (Fig. 7a) and CB-50 (Fig. 7b). The CB sample exhibited O_3 adsorption (1039 cm^{-1}) and O_2 adsorption (1261 cm^{-1}) features, along with a weaker peroxide intermediates (O_2^{2-} at 937 cm^{-1})

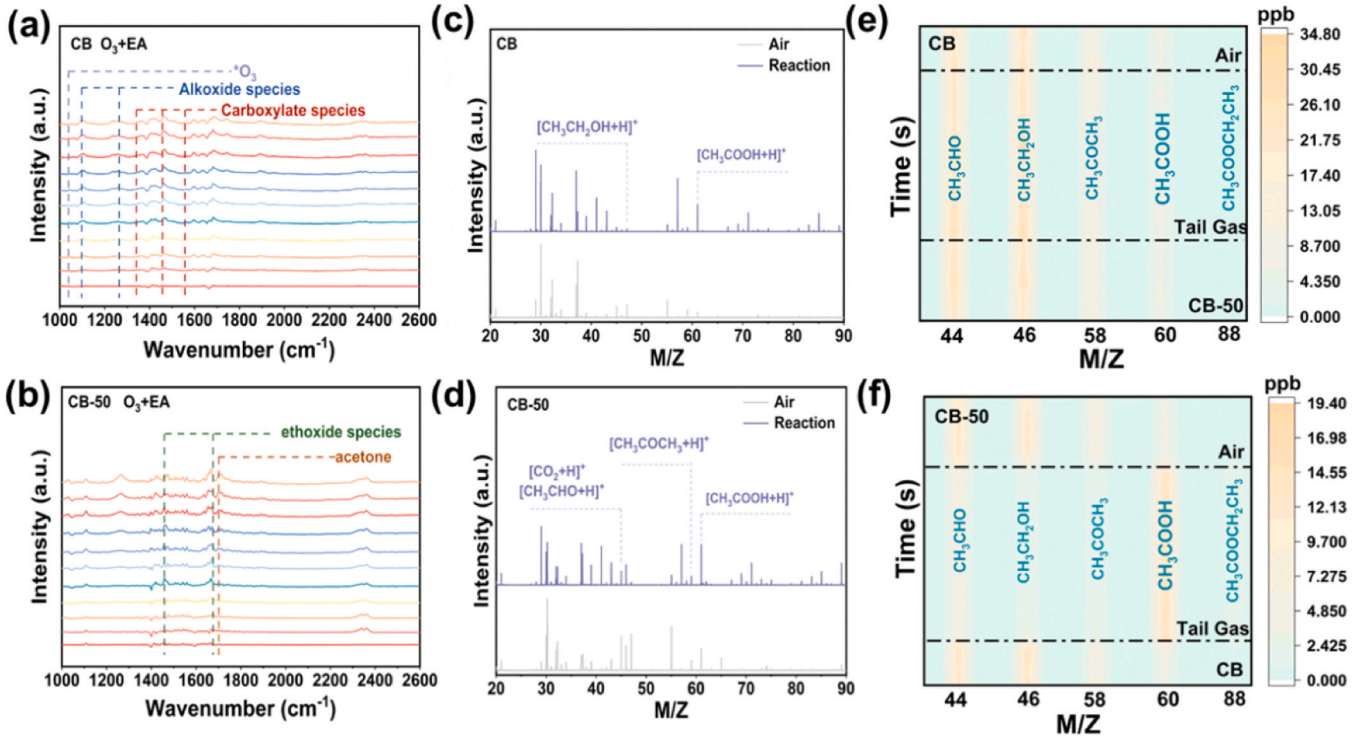

Fig. 8. Synergistic catalytic process of in-situ DRIFTS of (a) CB-50, (b) CB. PTR-TOF-MS spectra of (c) CB-50, (d) CB. Trace of ethyl acetate catalytic ozonation of (e) CB-50, (f) CB.

[42] In the contrast, on CB-50, distinct signals corresponding to O_3 activation products were observed, including atomic oxygen (*O at 860 cm^{-1}), peroxide intermediates (O_2^{2-} at 937 cm^{-1}), and adsorbed oxygen (*O_2 at 1271 cm^{-1}). No O_3 adsorption peaks were detected on CB-50, implying that O_3 was activated into reactive oxygen species ($O_3 \rightarrow *O + O_2^{2-}$). These results indicated that CB-50 possessed superior O_3 activation efficiency. Upon contact with O_3, CB-50 can rapidly decompose it into *O and O_2^{2-} species, which subsequently participated in the catalytic reaction. The enlarged *in-situ* DRIFTS spectra at 30 min in Fig. 7a-b have been redrawn to observe the intensity of O_2^{2-} species (Fig. 7e). The intensity of CB-50 at 937 cm^{-1} peak was much higher than those of CB, which means higher O_2^{2-}concentration of CB-50. Meanwhile, the EPR results showed that, under the same O_3 exposure time, a much stronger superoxide radical ($\bullet O_2^-$) signal was observed for the CB-50 system. The *in-situ* DRIFTS and EPR measurements consistently showed that CB-50 was more effective than CB in activating O_3 and generating ROS.

Through *in-situ* DRIFTS experiments under EA/air atmosphere (Figs. 7c, 7d), it was found that EA exhibited different adsorption patterns on CB and CB-50 catalysts. The spectra of the CB sample exhibited solely the characteristic peaks of EA at 1060 cm^{-1}, 1246 cm^{-1} (C-O-C asymmetric and symmetric acetate stretching) and 1693 cm^{-1} (C═O simplex stretching vibration). [43] This indicated that EA underwent only adsorption on CB without being converted into other intermediate species. For the spectra of CB-50, bands at 1091 and 1270 cm^{-1} were attributed to C-C and C-OH stretching vibrations of ethanol, respectively. The bands at 1561, 1458, and 1345 cm^{-1} were assigned to COO^- asymmetric stretching, C-H deformation, and COO^- symmetric stretching vibrations, respectively. These peaks corresponded to the interaction of EA with hydroxyl groups in CB-50, leading to the formation of ethanol and acetate. [44,45] In addition to the characteristic peaks of acetic acid and ethanol species, a significant CO_2 desorption peak at 2360 cm^{-1} was also observed. [46] This may be attributed to a decrease in the Cu^{2+} content, which led to a weakening of the binding capacity of the material for CO_2.

To understand the reaction mechanism and the intermediates generated during the synergistic catalysis, the *in-situ* DRIFTS technique was employed to elucidate the catalytic process on CB and CB-50 catalysts. CB exhibited the signals corresponding to carboxylic and alcoholic intermediates, along with a clear adsorbed O_3 (*O_3) peak, reflecting its limited ability to activate O_3 and degrade EA (Fig. 8a). Fig. 8b revealed the presence of acetaldehyde species on the CB-50 surface, characterized by the CH_2 scissoring vibration at 1457 cm^{-1} and the corresponding C═O stretching band at 1675 cm^{-1}. These results indicated that EA adsorption generated ethanol intermediates, which were then oxidized to acetaldehyde on the CB-50 surface upon O_3 exposure. Additionally, at 1695 cm^{-1}, carbonyl peak (C═O) belonging to the acetone species was observed, which could be converted from acetic acid ($2CH_3COOH \rightarrow CH_3COCH_3 + CO_2 + H_2O$). [43,47] No characteristic peaks of alcohol oxides or ROS were detected in CB-50. This indicated that the intermediates generated from O_3 activation and EA adsorption were fully involved in the synergistic catalysis and ultimately transformed into acetic acid and CO_2 as the final products. Such behavior can be attributed to the large specific surface area and well-developed pore structure of CB-50. These features facilitated the diffusion and transport of reactant molecules, thereby enhancing the contact between ROS and pollutant gases.

To characterize the gaseous products, the reaction gas was further analyzed using PTR-TOF-MS. Consistent with the *in-situ* DRIFTS results, signals at m/z = 45.03, 47.05, 59.05 and 61.03 were monitored, corresponding to acetaldehyde, ethanol, acetone, and acetic acid, respectively [48]. In the CB system (Fig. 8e), substantial amounts of acetaldehyde, ethanol, and trace acetone were detected in the reaction gas, indicating incomplete oxidation of EA and the limited oxidative activity of CB. In contrast, the CB-50 system (Fig. 8d) showed only a strong acetic acid signal. This indicated that ethanol, formed after EA adsorption, was rapidly oxidized to acetic acid. The latter was then further mineralized to CO_2 through synergistic catalysis.

Based on the combined results of *in-situ* DRIFTS and PTR-TOF-MS, a possible room-temperature synergistic catalytic pathway for EA and O_3

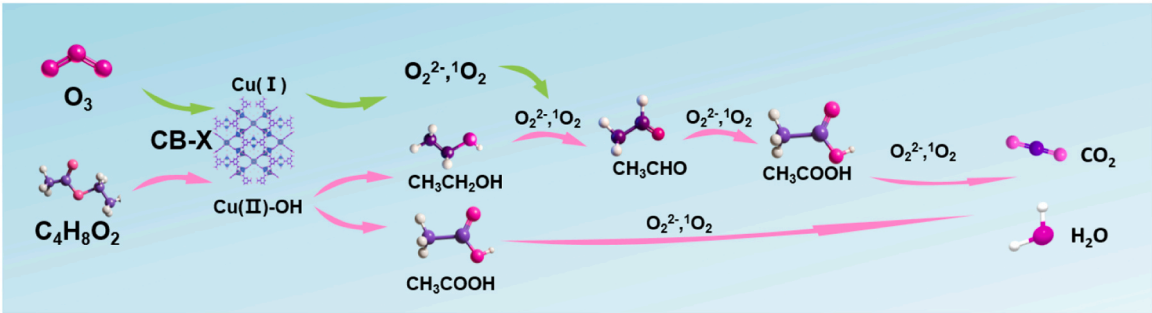

Scheme 2. Proposed synergistic catalytic mechanism for EA and O_3.

was proposed. In CB-50, O_3 was activated on Cu^+ sites and decomposed into *O and O_2^{2-} species, accompanied by oxidation of Cu^+ to Cu^{2+}. Subsequently, O_2^{2-} reacted with Cu^{2+} to generate $\bullet O_2^-$ and regenerate Cu^+. During adsorption, EA reacted with surface -OH groups to generate CH_3COO^- and $CH_3CH_2O^-$ intermediates. These intermediates were subsequently oxidized by O_2^{2-} and *O to acetic acid, which was finally mineralized into CO_2 and H_2O (Scheme 2).

$$2Cu^+ + O_3 \rightarrow *O + O_2^{2-} + 2Cu^{2+} \quad (2)$$

$$O_2^{2-} + Cu^{2+} \rightarrow \bullet O_2^- + Cu^+ \quad (3)$$

$$\bullet O_2^- + *O \rightarrow {}^1O_2 + *O^- \quad (4)$$

$$CH_3COOCH_2CH_3 + -OH \rightarrow CH_3COOH + *CH_3CH_2O \quad (5)$$

$$*CH_3CH_2O + *O^- \rightarrow CH_3CHO + OH^- \quad (6)$$

$$2CH_3CHO + {}^1O_2 \rightarrow 2CH_3COOH \quad (7)$$

$$CH_3COOH + 4*O \rightarrow 2CO_2 + H_2O \quad (8)$$

4. Conclusion

In summary, Cu-BTC MOFs were, for the first time, applied to the synergistic catalysis of gaseous EA and O_3. By applying defect engineering, we introduced tunable Cu(I)/Cu(II) dual sites into Cu-BTC, which enabled the simultaneous removal of high-concentration EA and low-concentration O_3 at room temperature. Cu(I) species served as primary active sites for O_3 activation to produce ROS such as *O and O_2^{2-}. Cu(II)-OH groups acted as the dominant adsorption sites for EA. CB-50 showed the highest catalytic activity, reaching 80 % EA removal and 77 % O_3 removal within 60 min, along with an EA mineralization rate of 90.3 %. Furthermore, universality experiments confirmed that defect engineering introduced low-valent metal centers into representative MOFs, validating their role in O_3 activation. This study offers mechanistic insights and guidance for the rational design of advanced catalysts for OVOC–O_3 synergistic catalysis.

Environmental implication

This work demonstrates that defect-engineered Cu-BTC with tunable Cu(I)/Cu(II) dual sites enables efficient room-temperature synergistic catalysis of coexisting EA and O_3. The dual-site mechanism enhances catalyst–pollutant interactions while reducing energy consumption, providing practical guidance for OVOCs and O_3 pollution control in complex environments.

CRediT authorship contribution statement

Kaihuang Zhu: Conceptualization. **Xiao Wang:** Writing – original draft, Conceptualization. **Guanqing Song:** Methodology, Conceptualization. **Xinge Li:** Writing – original draft, Methodology, Investigation, Formal analysis, Data curation, Conceptualization. **Yan Wang:** Writing – review & editing, Visualization, Supervision, Funding acquisition, Conceptualization. **Jing Sun:** Writing – review & editing, Funding acquisition. **Xinhong Xu:** Resources, Funding acquisition. **Xiaomeng Ren:** Funding acquisition. **Gansheng Shi:** Formal analysis. **Guanhong Lu:** Formal analysis. **Shijie Yang:** Writing – original draft, Formal analysis, Conceptualization.

Declaration of Competing Interest

The authors declare that they have no known competing financial interests or personal relationships that could have appeared to influence the work reported in this paper

Acknowledgments

This work was financially supported by the funding from the State Key Laboratory of High Performance Ceramics.

Appendix A. Supporting information

Supplementary data associated with this article can be found in the online version at doi:10.1016/j.jhazmat.2025.140882.

Data Availability

Data will be made available on request.

References

[1] Kwon, H., Seo, S.W., Kim, T.G., Lee, E.S., Lanh, P.T., Yang, S., Ryu, S., Kim, J.W., 2016. Ultrathin and flat layer black phosphorus fabricated by reactive oxygen and water rinse. ACS Nano 10, 8723–8731. https://doi.org/10.1021/acsnano.6b04194.

[2] Yu, C., Parikh, A.N., Groves, J.T., 2005. Direct patterning of membrane-derivatized colloids using in-situ uv-ozone photolithography. Adv Mater 17, 1477–1480. https://doi.org/10.1002/adma.200401586.

[3] Rao, P., Yu, Y., Wang, S., Zhou, Y., Wu, X., Li, K., Qi, A., Deng, P., Cheng, Y., Li, J., Miao, Z., Tian, X., 2024. Understanding the improvement mechanism of plasma etching treatment on oxygen reduction reaction catalysts. Exploration 4, 20230034. https://doi.org/10.1002/EXP.20230034.

[4] Park, S., Choe, W., Jo, C., 2018. Interplay among ozone and nitrogen oxides in air plasmas: Rapid change in plasma chemistry. Chem Eng J 352, 1014–1021. https://doi.org/10.1016/j.cej.2018.07.039.

[5] Bo, Z., Yu, K., Lu, G., Mao, S., Chen, J., Fan, F., 2010. Nanoscale discharge electrode for minimizing ozone emission from indoor corona devices. Environ Sci Technol 44, 6337–6342. https://doi.org/10.1021/es903917f.

[6] Kask, M., Bolobajev, J., Krichevskaya, M., 2020. Gas-phase photocatalytic degradation of acetone and toluene, and their mixture in the presence of ozone in continuous multi-section reactor as possible air post-treatment for exhaust from pulsed corona discharge. Chem Eng J 399, 125815. https://doi.org/10.1016/j.cej.2020.125815.

[7] Liu, B., Ji, J., Zhang, B., Huang, W., Gan, Y., Leung, D.Y.C., Huang, H., 2022. Catalytic ozonation of VOCs at low temperature: a comprehensive review. J Hazard Mater 422, 126847. https://doi.org/10.1016/j.jhazmat.2021.126847.

[8] Chen, G., Wang, Z., Lin, F., Zhang, Z., Yu, H., Yan, B., Wang, Z., 2020. Comparative investigation on catalytic ozonation of VOCs in different types over supported

MnO*x* catalysts. J Hazard Mater 391, 122218. https://doi.org/10.1016/j.jhazmat.2020.122218.
[9] Lin, F., Zhang, Z., Xiang, L., Zhang, L., Cheng, Z., Wang, Z., Yan, B., Chen, G., 2022. Efficient degradation of multiple Cl-VOCs by catalytic ozonation over MnO*x* catalysts with different supports. Chem Eng J 435, 134807. https://doi.org/10.1016/j.cej.2022.134807.
[10] Kim, J., Lee, J.E., Lee, H.W., Jeon, J.-K., Song, J., Jung, S.-C., Tsang, Y.F., Park, Y.-K., 2020. Catalytic ozonation of toluene using Mn–M bimetallic HZSM-5 (M: Fe, Cu, Ru, Ag) catalysts at room temperature. J Hazard Mater 397, 122577. https://doi.org/10.1016/j.jhazmat.2020.122577.
[11] Xu, Z., Mo, S., Li, Y., Zhang, Y., Wu, J., Fu, M., Niu, X., Hu, Y., Ye, D., 2022. Pt/MnOx for toluene mineralization via ozonation catalysis at low temperature: SMSI optimization of surface oxygen species. Chemosphere 286, 131754. https://doi.org/10.1016/j.chemosphere.2021.131754.
[12] Su, M., Zhang, H., Zhang, P., 2025. Tuning ozone decomposition intermediates on δ-MnO2 to improve its moisture-resistance in ozone catalytic oxidation of toluene. Appl Catal B Environ Energy 378, 125526. https://doi.org/10.1016/j.apcatb.2025.125526.
[13] Rezaei, F., Moussavi, G., Bakhtiari, A.R., Yamini, Y., 2016. Toluene removal from waste air stream by the catalytic ozonation process with MgO/GAC composite as catalyst. J Hazard Mater 306, 348–358. https://doi.org/10.1016/j.jhazmat.2015.11.026.
[14] Shao, Q., Cheng, Z., Gao, L., Li, T., Zhang, J., Long, C., 2023. Tuning the properties of oxygen vacancy around Cu-Mn mixed oxides on dealumination Y zeolite by P-doping to achieve ultra-efficient catalytic ozonation of toluene with low ozone consumption. Appl Catal B Environ 339, 123154. https://doi.org/10.1016/j.apcatb.2023.123154.
[15] Liang, L., Cao, P., Bai, H., Du, X., Chen, S., Yu, H., Liu, Y., Su, Y., Quan, X., 2025. Role of curvature in modulating electronic structure of active sites on hollow carbon spheres for efficient decontamination in catalytic ozonation process. Appl Catal B Environ Energy 366, 125067. https://doi.org/10.1016/j.apcatb.2025.125067.
[16] Ye, Z., Wang, G., Giraudon, J., Nikiforov, A., Chen, J., Zhao, L., Zhang, X., Wang, J., 2022. Investigation of Cu-Mn catalytic ozonation of toluene: Crystal phase, intermediates and mechanism. J Hazard Mater 424, 127321. https://doi.org/10.1016/j.jhazmat.2021.127321.
[17] Sun, Y., Liu, P., Wang, Z., Tang, H., He, Y., Zhu, Y., 2023. Efficient catalytic ozonation of ethyl acetate over Cu-Mn catalysts: Further insights into the reaction mechanism. Chem Eng J 477, 147282. https://doi.org/10.1016/j.cej.2023.147282.
[18] Dong, C., Yang, J.-J., Xie, L.-H., Cui, G., Fang, W.-H., Li, J.-R., 2022. Catalytic ozone decomposition and adsorptive VOCs removal in bimetallic metal-organic frameworks. Nat Commun 13, 4991. https://doi.org/10.1038/s41467-022-32678-2.
[19] Wang, H., Rassu, P., Wang, X., Li, H., Wang, X., Wang, X., Feng, X., Yin, A., Li, P., Jin, X., Chen, S.-L., Ma, X., Wang, B., 2018. An Iron-Containing Metal–Organic Framework as a Highly Efficient Catalyst for Ozone Decomposition. Angew Chem Int Ed 57, 16416–16420. https://doi.org/10.1002/anie.201810268.
[20] Wang, Q.-N., Duan, R., Feng, Z., Zhang, Y., Luan, P., Feng, Z., Wang, J., Li, C., 2024. Understanding the synergistic catalysis in hydrogenation of carbonyl groups on Cu-Based Catalysts. ACS Catal 14, 1620–1628. https://doi.org/10.1021/acscatal.3c04740.
[21] Guo, Y., Feng, C., Wang, S., Xie, Y., Guo, C., Liu, Z., Akram, N., Zhang, Y., Zhao, Y., Wang, J., 2020. Construction of planar-type defect-engineered metal–organic frameworks with both mixed-valence sites and copper-ion vacancies for photocatalysis. J Mater Chem A 8, 24477–24485. https://doi.org/10.1039/D0TA08085C.
[22] Wang, W., Sharapa, D.I., Chandresh, A., Nefedov, A., Heißler, S., Heinke, L., Studt, F., Wang, Y., Wöll, C., 2020. Interplay of Electronic and Steric Effects to Yield Low-Temperature CO Oxidation at Metal Single Sites in Defect-Engineered HKUST-1. Angew Chem Int Ed 59, 10514–10518. https://doi.org/10.1002/anie.202000385.
[23] Song, G., Shi, G., Chen, L., Wang, X., Sun, J., Yu, L., Xie, X., 2022. Different degradation mechanisms of low-concentration ozone for MIL-100(Fe) and MIL-100 (Mn) over wide humidity fluctuation. Chemosphere 308, 136352. https://doi.org/10.1016/j.chemosphere.2022.136352.
[24] Chen, L., Wang, X., Shi, G., Lu, G., Wang, Y., Xie, X., Chen, D., Sun, J., 2023. The regulation of Lewis acid/basic sites in NaFe bimetal MOXs for the controllable photocatalytic degradation of electron-rich/deficient VOCs. Appl Catal B Environ 334, 122850. https://doi.org/10.1016/j.apcatb.2023.122850.
[25] Schlichte, K., Kratzke, T., Kaskel, S., 2004. Improved synthesis, thermal stability and catalytic properties of the metal-organic framework compound Cu3(BTC)2. Microporous Mesoporous Mater 73, 81–88. https://doi.org/10.1016/j.micromeso.2003.12.027.
[26] He, K., Chen, N., Wang, C., Wei, L., Chen, J., 2018. Method for Determining Crystal Grain Size by X-Ray Diffraction. Cryst Res Technol 53, 1700157. https://doi.org/10.1002/crat.201700157.
[27] Zhang, L., Guo, C., Chen, T., Guo, Y., Hassan, A., Kou, Y., Guo, C., Wang, J., 2022. Effects of different defective linkers on the photocatalytic properties of Cu-BTC for overall water decomposition. Appl Catal B Environ 303, 120888. https://doi.org/10.1016/j.apcatb.2021.120888.
[28] Petit, C., Levasseur, B., Mendoza, B., Bandosz, T.J., 2012. Reactive adsorption of acidic gases on MOF/graphite oxide composites. Microporous Mesoporous Mater 154, 107–112. https://doi.org/10.1016/j.micromeso.2011.09.012.
[29] Chen, Z., He, X., Ge, J., Fan, G., Zhang, L., Parvez, A.M., Wang, G., 2022. Controllable fabrication of nanofibrillated cellulose supported HKUST-1 hierarchically porous membranes for highly efficient removal of formaldehyde in air. Ind Crops Prod 186, 115269. https://doi.org/10.1016/j.indcrop.2022.115269.
[30] Sun, D., Chen, L., Zeng, L., Shi, X., Lu, J., 2022. Quasi-Cu-MOFs: highly improved water stability and electrocatalytic activity toward H2O2 reduction among pristine 3D MOFs. J Mater Chem A 11, 31–40. https://doi.org/10.1039/D2TA05833B.
[31] Yang, S., Yu, J., Lu, G., Song, G., Shi, G., Wang, Y., Xie, X., Yuan, H., Ren, X., Sun, J., 2024. Effect of NH2-functionalization of MIL-125 on photocatalytic degradation of o-xylene and acetaldehyde. Chem Eng J 498, 155251. https://doi.org/10.1016/j.cej.2024.155251.
[32] Kim, S.-Y., Kim, A.-R., Yoon, J.W., Kim, H.-J., Bae, Y.-S., 2018. Creation of mesoporous defects in a microporous metal-organic framework by an acetic acid-fragmented linker co-assembly and its remarkable effects on methane uptake. Chem Eng J 335, 94–100. https://doi.org/10.1016/j.cej.2017.10.078.
[33] He, Y., Li, C., Chen, X.-B., Shi, Z., Feng, S., 2022. Visible-Light-Responsive UiO-66 (Zr) with defects efficiently promoting photocatalytic CO_2 Reduction. ACS Appl Mater Interfaces 14, 28977–28984. https://doi.org/10.1021/acsami.2c06993.
[34] Mo Z., Wang S., Hui Y., Kong W., Zhai P., Wang H., Zu Y., Qin Y., Song L. Enhanced Adsorption Desulfurization Performance over CuCeY Zeolites Prepared by Low-Temperature Calcination under H2 Atmosphere. https://doi.org/10.1002/slct.202002498.
[35] Zhou, X., Ke, M.-K., Huang, G.-X., Chen, C., Chen, W., Liang, K., Qu, Y., Yang, J., Wang, Y., Li, F., Yu, H.-Q., Wu, Y., 2022. Identification of Fenton-like active Cu sites by heteroatom modulation of electronic density. Proc Natl Acad Sci 119, e2119492119. https://doi.org/10.1073/pnas.2119492119.
[36] Platero, F., López-Martín, A., Caballero, A., Rojas, T.C., Nolan, M., Colón, G., 2021. Overcoming Pd–TiO2 Deactivation during H2 Production from Photoreforming Using Cu@Pd Nanoparticles Supported on TiO2. ACS Appl Nano Mater 4, 3204–3219. https://doi.org/10.1021/acsanm.1c00345.
[37] Liu, Y., Chen, G., Chen, J., Niu, H., 2022. Excellent catalytic performance of Ce–MOF with abundant oxygen vacancies supported noble metal pt in the oxidation of toluene. Catalysts 12, 775. https://doi.org/10.3390/catal12070775.
[38] Sun, Z.-B., Si, Y.-N., Zhao, S.-N., Wang, Q.-Y., Zang, S.-Q., 2021. Ozone decomposition by a manganese-organic framework over the entire humidity range. J Am Chem Soc. https://doi.org/10.1021/jacs.1c01027.
[39] Zhu, Y., Yang, L., Ma, J., Fang, Y., Yang, J., Chen, X., Zheng, J., Zhang, S., Chen, W., Pan, C., Zhang, B., Qiu, X., Luo, Z., Wang, J., Guo, Y., 2023. Rapid Ozone Decomposition over Water-activated Monolithic MoO3/Graphdiyne Nanowalls under High Humidity. Angew Chem Int Ed 62, e202309158. https://doi.org/10.1002/anie.202309158.
[40] Wang, Y., Zhou, Y., Sun, W., Wang, X., Yao, J., Li, H., 2024. Identifying radical pathways for Cu(I)/Cu(II) relay catalyzed oxygenation via online coupled EPR/UV–Vis/Near-IR Monitoring. Adv Sci 11, 2402890. https://doi.org/10.1002/advs.202402890.
[41] Xiang, L., Lin, F., Cai, B., Li, G., Zhang, L., Wang, Z., Yan, B., Wang, Y., Chen, G., 2022. Catalytic ozonation of CH2Cl2 over hollow urchin-like MnO2 with regulation of active oxygen by catalyst modification and ozone promotion. J Hazard Mater 436, 129217. https://doi.org/10.1016/j.jhazmat.2022.129217.
[42] Liu, X., Shi, Y., Yu, L., Zhan, G., Chen, Z., Zhou, B., Zhang, H., Li, H., Liu, X., Zhang, L., Ai, Z., 2025. Bifunctional-boron incorporated mesocrystalline CeO2 for enhanced catalytic ozonation benzene at room temperature. Appl Catal B Environ Energy 371, 125245. https://doi.org/10.1016/j.apcatb.2025.125245.
[43] Phung, T.K., Casazza, A.A., Aliakbarian, B., Finocchio, E., Perego, P., Busca, G., 2013. Catalytic conversion of ethyl acetate and acetic acid on alumina as models of vegetable oils conversion to biofuels. Chem Eng J 215216 838–848. https://doi.org/10.1016/j.cej.2012.11.057.
[44] Lao, Y.-J., Jiang, X.-X., Huang, J., Zhang, Z., Wang, X.-Y., 2021. Catalytic oxidation of ethyl acetate on Ce–Mn–O catalysts modified by La. Rare Met 40, 547–554. https://doi.org/10.1007/s12598-019-01357-5.
[45] Li, J., Mo, S., Ding, X., Huang, L., Zhou, X., Fan, Y., Zhang, Y., Fu, M., Xie, Q., Ye, D., 2023. Hollow cavity engineering of MOFs-derived hierarchical MnOx structure for highly efficient photothermal degradation of ethyl acetate under light irradiation. Chem Eng J 464, 142412. https://doi.org/10.1016/j.cej.2023.142412.
[46] Liao, H., Huang, K., Hou, W., Guo, H., Lian, C., Zhang, J., Liu, Z., Wang, L., 2024. Atmosphere engineering of metal-free Te/C3N4 p-n heterojunction for nearly 100% photocatalytic converting CO2 to CO. Adv Powder Mater 3, 100243. https://doi.org/10.1016/j.apmate.2024.100243.
[47] Lao, Y.-J., Jiang, X.-X., Huang, J., Zhang, Z., Wang, X.-Y., 2021. Catalytic oxidation of ethyl acetate on Ce–Mn–O catalysts modified by La. Rare Met 40, 547–554. https://doi.org/10.1007/s12598-019-01357-5.
[48] Yang, S., Yu, J., Lu, G., Song, G., Shi, G., Wang, Y., Xie, X., Yuan, H., Ren, X., Sun, J., 2024. Effect of NH2-functionalization of MIL-125 on photocatalytic degradation of o-xylene and acetaldehyde. Chem Eng J 498, 155251. https://doi.org/10.1016/j.cej.2024.155251.